CHAPTER 2

THEORY AND NUMERICAL INVESTIGATIONS OF GYRO-TWYSTRON AMPLIFIER*

*Part of this work has been published as:

Vangalla Veera Babu, M. Thottappan, and Smrity Dwivedi " Design and simulation investigations of a high gain millimeter wave gyro-twystron amplifier," *Journal of Electromagnetic Waves and Applications*, vol. 36, no. 18, pp. 2740-2755, July 2022, doi:10.1080/09205071.2022.2106448.

2.1. Introduction

The evolution, physics, and classification of microwave tubes up to the gyro-twystron are discussed in the previous chapter. The CRM mechanism-based gyro devices and their fundamental operational principles are examined in more detail, leading to a review of the gyro-Twystron. However, gyro-twystron literature reviews are restricted to reporting performance metrics, scope, and limitations and also suggested it as a potential application in millimeter-wave high-resolution radar systems. A *Ka*-band gyro-twystron is analyzed with a nonlinear multimode analysis to study the behavior of its beam-wave interaction, the stability of the amplifier against the parasitic oscillations is studied using linear theory, and the design methodology of the interaction circuit is discussed in the present chapter.

Gyro- twystron RF input cavity section and output waveguide section are analogous to gyro-klystron and gyro-TWT, respectively, as reflected in existing mathematical formalism. Different design approaches are taken from the parental gyro-amplifiers of gyro-twystron, and gyro-amplifiers literature is reformed to develop a gyro-twystron design methodology. Chu et al. devised a design technique for the gyroklystron amplifier in 1985, and the design investigations include the selection of operating mode, frequency, wall loss, and space charge effects. After, in 2000, numerous gyroklystron tubes were developed using the MAGYKL code. Gyro-TWT has a more straightforward interaction structure, namely a cylindrical waveguide. However, the gyro-TWT operation is complicated and susceptible to oscillations induced by both internal and external feedback mechanisms. As a result, designing a stable RF interaction structure is a significant impediment in gyro-TWT. The operational mechanism of gyro-TWT is examined using the dispersion curve to assure the zone of convective instability and identify competing or backward-wave modes to

explore absolute instability. The computation of the critical length of backward wave modes is required to design gyro-TWT because the waveguide length must be kept less than the critical length of backward wave modes to ensure stable operation. With these developments in gyroklystron and gyro-TWT design approaches, we deduced and established gyro-twystron design approach.

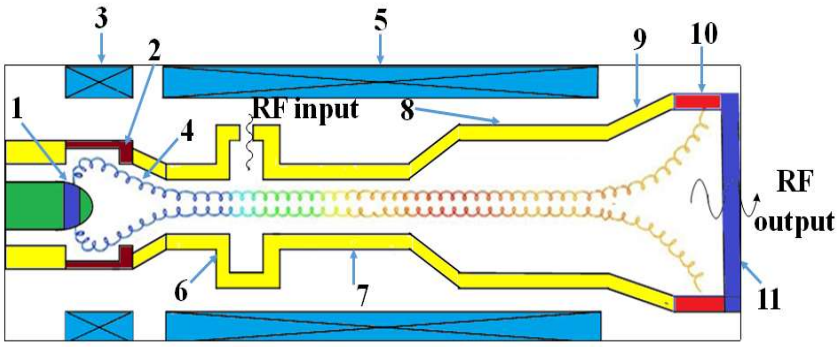

1. Particle Emitter 2. Anode 3. Gun Solenoid 4. Compression Zone 5. Main Solenoid 6. Input Cavity 7. Drift Tube 8. Output Waveguide 9. Up Taper 10. Particle Collector 11. RF Output Window

Fig. 2. 1. Schematic diagram of gyro-twystron.

2.2. Design of Interaction Circuit

The gyro-twystron design approach is governed by the physics and principle of VEDs. The electromagnetic behavior of each component of the gyro-twystron has been investigated in the presence and absence of an electron beam in order to establish the design process, which includes the selection of the desired mode, electron beam parameters, and magnetic field operation. Desired goals and performance metrics drive the design approach since they are the starting point for design calculations. The initial step was to determine the RF dimension to support an EM wave's desired mode and frequency. The second phase involves incorporating electron beam parameters into design calculations; for example, the start oscillation current is a function of the quality factor. Designing a hybrid interaction structure for beam-wave interaction is complex,

and each section of the gyro-twystron is designed independently to simplify the design procedure. Each section design approach is described in detail below.

2.2.1. Input Cavity

The contemporary design of a single cavity followed by an output waveguide collectively treated as RF interaction circuit is displayed in Figure 2.1. It comprises three sections involving modulation in the input resonant cylindrical cavity, ballistic phase bunching in the field-free drift section, and beam wave interaction in non-resonant output circular waveguide. The design of a hybrid amplifier RF structure depends on different parameters like operating frequency, operating mode, and beam parameters. The dimensions of the RF input cavity are computed with the desired frequency and mode, which is given by

$$r_c = x_{mn}\lambda / 2\pi \tag{2.1}$$

where, x_{mn} is the Eigenvalue of TE_{mn} mode, λ is the operating wavelength. The resonating frequency (f_r) of TE_{mnd} mode in the a cylindrical cavity is determined by

$$f_r = \left(\frac{c}{2\pi}\right)\left(\sqrt{\left(\frac{x_{mn}}{r_c}\right)^2 + \left(\frac{d\pi}{L_c}\right)}\right) \tag{2.2}$$

The cavity length and radius are optimized to attain the required resonant frequency. The unloaded cavity resonating frequency is kept slightly higher while the dielectric loading decreases the resonating frequency. The cavity is loaded with dielectric material to reduce the quality factor and enhance the start oscillation current. For steady operation, the beam current is kept lower than the cavity start oscillation current (SOC), [100] which is calculated as follows:

$$I_{st} = (\pi/2)^{5/2}\frac{c^3 m_e \varepsilon_0}{e}\left(\frac{2^s s!}{s^s}\right)\frac{\beta_{t0}^{-2(3-s)}\gamma_0}{Q}\frac{L_c\left(4/\pi\mu^2\right)\left[e^{2x^2}/(\mu x - s)\right]}{\lambda C_{mn}} \tag{2.3}$$

The dielectric ring is loaded in the cavity to obtain a preferred quality factor (*Q*-factor) with reduced oscillations in the output signal power. This results in good stability since the cavity is now operating below the start oscillation current (SOC) [43]. A *Q*-factor of ~200 is selected for the input cavity to have minimal oscillations in the proposed design. However, as shown in Figure 2. 2, even for higher quality factors (above 200) the SOC is well above 15A for a range of magnetic field (1.1 T–1.30 T), which is higher than the chosen operating current of 10 A, thus ensuring the stable operation of the device.

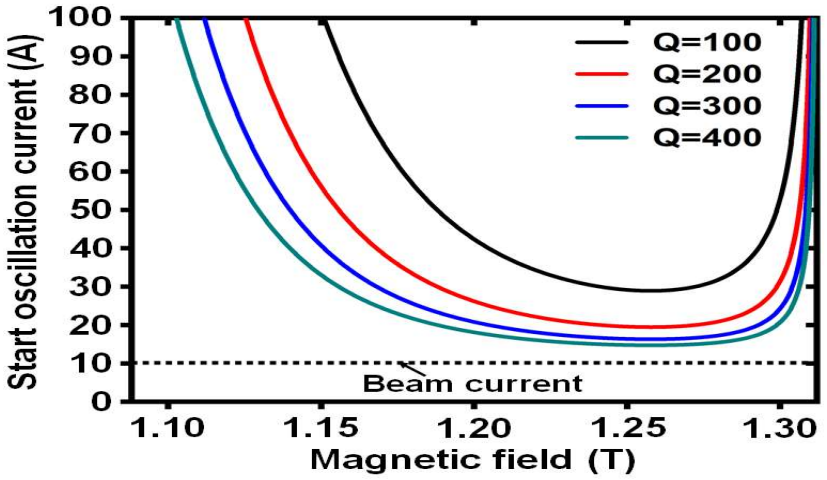

Fig. 2. 2. SOC variation with the magnetic field for different quality factors (Q=100, Q=200, Q=300, and Q=400) at the input cavity.

2.2.2. Drift Tube

One practical design constraint that governs device design is isolation between adjacent components. The field-free drift tube is designed to achieve the required isolation between adjacent cavities followed by waveguide. The drift tube dimensions are chosen to enable excellent isolation while avoiding beam interception with the drift tube wall. The drift section is selected to provide cut-off to TE_{01} mode and also to satisfy the condition for the drift radius $r_b < r_d < r_c$ to avoid the field propagation, where,

r_b is electron beam guiding radius, r_d is drift tube radius, and r_c is cavity radius. The drift tube length (L_d) is chosen by cold cavity dispersion relation [29] is

$$L_d > 5.75 \Big/ \left[\left(x_{m_k n_k} / r_d \right)^2 - \left(\omega / c \right)^2 \right]^{1/2} \tag{2.4}$$

where, ω and r_d are the angular operating frequency and drift tube radius, respectively. TE_{11} mode is unsuitable for high-power operation due to its lower transverse dimension, which causes beam interception in the drift tube. The TE_{01} mode has a high eigenvalue than the TE_{11} mode. It gives a larger transverse dimension, which minimizes the space charge effect and beam interception and lowers wall loss via azimuthal symmetry. To cut off the operating TE_{01} mode, the immediate lower mode TE_{21} is selected. To suppress the TE_{11} mode, the length of the drift tube is enlarged, and it is extensively loaded with dielectric rings.

2.2.3. Output Waveguide

In a hybrid amplifier, the RF wave and electrons are interacting in the non-resonant output waveguide region. The length of the output waveguide is determined by the minimum beam current value at which oscillation originates. Oscillations in the output waveguide section of amplifiers occur due to the internal feedback mechanism of absolute instability. In gyro-traveling wave amplifiers, beam-wave interaction is based on convective instability. However, the device operating at a high current, this convective instability transforms into absolute instability. To prevent absolute instability, beam parameters are carefully chosen. The absolute instability is investigated using the dispersion equation,

$$\left(\omega^2 - c^2\left(k_z^2 + k_{mn}^2\right)\right)\left(\omega - k_z v_z - s\Omega/\gamma\right)^2 = \frac{-4I_b\beta_\perp^2\left(J_n'\left(k_\perp r_g\right)\times\left(J_n'\left(k_\perp r_L\right)\right)\right)^2}{\gamma_0\beta_\parallel I_A\left(x_{mn}^2 - m^2\right)J_m^2\left(x_{mn}\right)} \quad (2.5)$$

where I_b is beam current , ω angular frequency, k_z axial wave number, $k_{mn} = x_{mn}/r_w$, x_{mn} is nth root of $J_m'\left(x_{mn}\right) = 0$, $\beta_\perp$ normalized velocity, I_A is Alfven current, $\gamma_0 = \left(1 - \beta_\parallel^2 - \beta_\perp^2\right)^{-\frac{1}{2}}$, $\Omega = \frac{eB_0}{m_e}$, r_g, r_L and r_w are guiding radius, Larmor radius and wall radius, respectively.

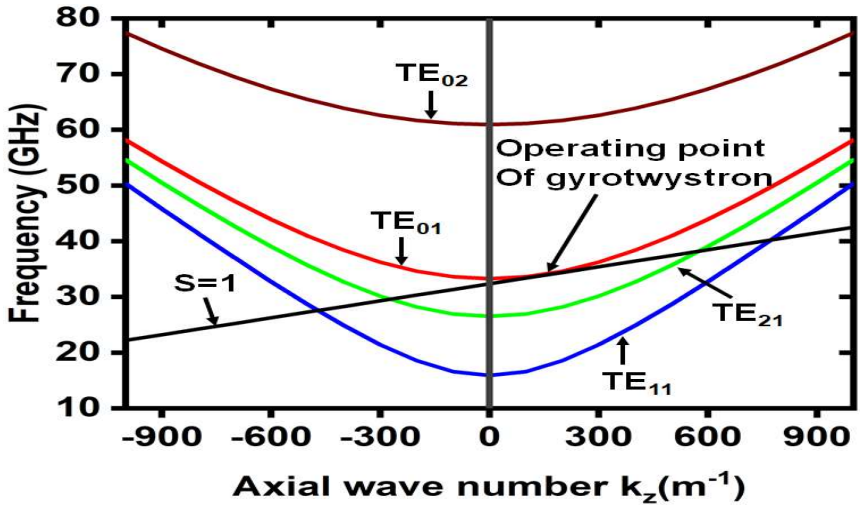

Fig. 2. 3. Dispersion diagram of *Ka*-band gyro-twystron.

The *Ka*-band gyro-twystron amplifier's operating characteristics are discussed through the dispersion diagram, as shown in Figure 2. 3 that are attained by solving the dispersion equations of waveguide and beam modes. As shown in Figure 2. 3, the slope of the waveguide mode curve gives the phase velocity of the wave. The first harmonic (s = 1) line touches the waveguide operating TE_{01} mode in the positive k_z region at 35GHz. It also intersects with TE_{21} and TE_{11} modes in the k_z negative region, known as backward-wave modes, competing with desired operating TE_{01} mode. After solving the dispersion relation, the threshold limit of current (SOC) and waveguide length (SOL)

for the beginning of absolute instability can be calculated [122]. The current gyro-interaction twystron length is optimized using Eqn. 2.6 for a beam parameter of 65 kV, 10 A, and an operating mode and frequency of TE_{01} and 35 GHz, respectively.

$$L_w = \left\{ \frac{4\gamma_0 k_z I_A \beta_{\parallel}^3 J_m^2\left(x_{mn}\right)\left(x_{mn}^2 - m^2\right)}{k_{\perp}^4 I \beta_{\perp}^2 \left(J_n\left(k_{\perp} r_L\right)\left(J_{m\pm s}\left(k_{\perp} r_g\right)\right)\right)} \right\}^{\frac{1}{3}} \tag{2.6}$$

For the stable device operation, the beam current should be lower than the start oscillation current. The waveguide's length is chosen smaller than the Start Oscillation Length (SOL) of the competing modes [86]. SOC and SOL of the backward-wave modes in the interaction structure, including TE_{11}, TE_{02}, and TE_{21}, are estimated from the small-signal analysis of gyro TWT. Figure 2.4. (a) Depicts the SOCs as a function of length for backward-wave modes. It shows the TE_{02} mode has the least start oscillation length for the desired operation. Therefore, for steady operation of the gyro-twystron, the output waveguide length must be below the SOL of TE_{02} mode. Figure 2.4. (b) Shows the SOC of desired mode decreases as the velocity ratio (α) increases. The start oscillation current of gyro-twystron is strongly depends on to the pitch factor(α), as it increases the transverse moment of electrons, which in turn reduces SOC [122]. A careful increment in pitch factor is required to enhance the kinetic energy of the electron, resulting in more amplification of the RF signal.

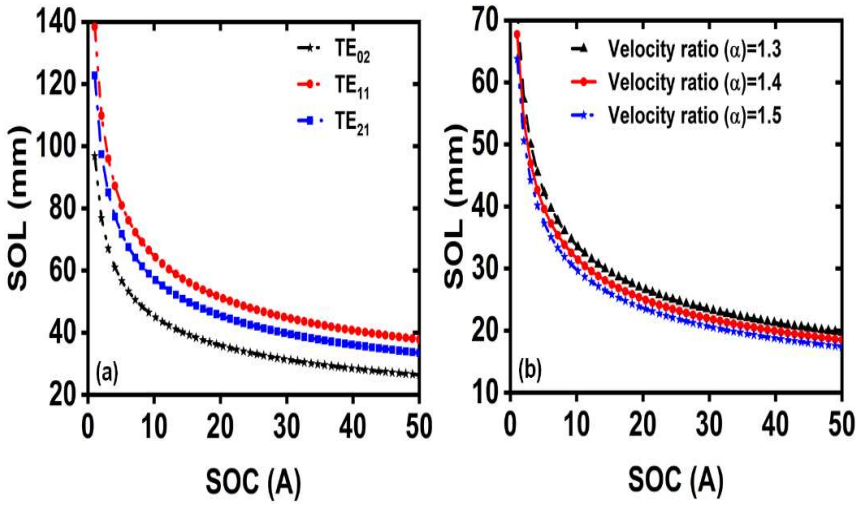

Fig. 2. 4. (a) SOC versus SOL of competing modes **(b)** SOC for the TE_{01} mode with different velocity ratio(α).

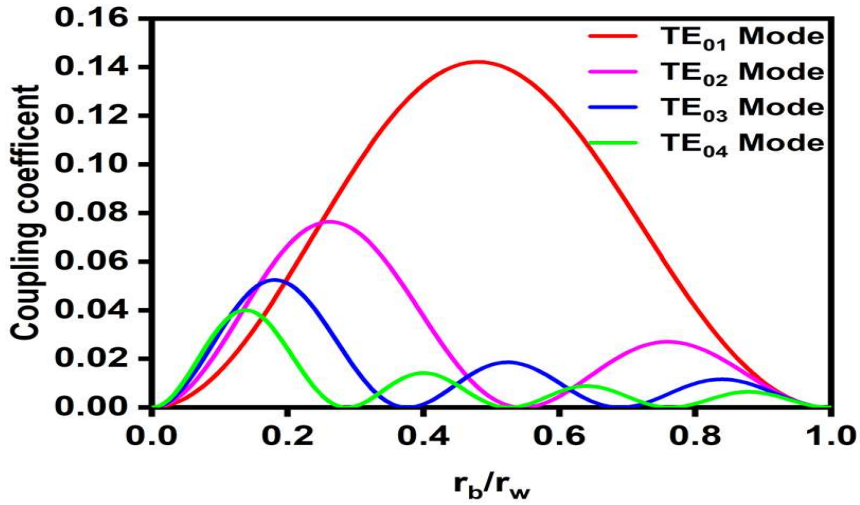

Fig. 2. 5. Coupling coefficient versus guiding center radius.

To achieve the maximum performance, an effective beam wave coupling is required [123], which is defined as coupling coefficient (C_{mn})

$$C_{mn} = \frac{J_{m\pm s}^2\left(k_\perp r_b\right)}{J_m^2\left(x_{mn}\right)\left(x_{mn}^2 - m^2\right)} \tag{2.7}$$

C_{mn} is depends on the gyrating beam positioning and transverse electric field. From the coupling coefficient expression, we can find the optimum electron beam launching position to have maximum coupling for the chosen mode. For the maximum coupling the beam radius and the guiding center radius is chosen as it gives the best beam wave

coupling as well as it avoids the interception with the structure wall especially in drift tubes, which are having smaller radius. The coupling strength of operating and backward-wave modes concerning the beam position is shown in Figure 2.5. and it is observed that the operating TE_{01} mode has the maximum coupling of the RF wave and beam occurs at $0.48r_w$. The operating TE_{01} mode has the maximum coupling.

2.3. Multimode Nonlinear Analysis

Nonlinear analysis is used to investigate the behavior of beam-wave interaction in the presence of electromagnetic fields supporting the interaction structure. The present nonlinear theory is more generic and applies to any gyro-twystron amplifiers operating at any cyclotron harmonic and transverse electric modes. The process of beam-wave interaction is basically dependent on the synchronism of the cyclotron frequencies of the gyrating electron beam and the operating frequency of the applied input signal. Our study begins with Maxwell's equation, which represents the field components of the TE_{mn} mode excited in the circular waveguide. A source present term is included in the wave equation to account for the effect of the electron beam. Furthermore, in order to derive the wave equations in terms of the slow time scale variables, the coordinates must be transformed from the cylindrical system to the guiding center system. Graf's summation theorem for Bessel's functions can be used to incorporate this modification. Finally, circuit equations determine the magnitude and phase of electromagnetic fields. The relativistic Lorentz force equation is used to explain electron beam dynamics, which determine electron velocity and RF wave propagation in the presence of an axial magnetic field (assuming space charge fields are minimal). There are a few key assumptions made in this analysis: (1) that all electrons have the same kinetic energy or are mono-energetic at the beginning of the interaction structure; and (2) that space charge effects in the interaction structure are neglected. (3)

All particles entering the interaction region separated by integral multiples of the wave period will follow similar trajectories.

Interaction circuit is the region where the electron beam interacts with RF wave and thereby growth of RF energy occurs. The energy conversion process in the RF interaction circuit of gyro-twystron is explained by taking into account the interaction of the annular electron beam with the RF wave at the cavity and by the interaction of the bunched electron beam with the forward travelling wave at the output cylindrical waveguide. The electron beam dynamics in the cavity and waveguide sections are explained in detail as follows:

2.3.1 Electron Beam Dynamics in the Cavity

In the present hybrid device RF structure, the formalism for the input cavity is derived from the small-signal theory [103]. Electron motion is disturbed by a small RF field at the cavity described by the normalized energy (w), momentum, (p) and phase (θ) over the normalized axial length (ς), which are written as

$$\frac{dw}{d\varsigma} = \frac{p^{s_k}}{p_z}\mathrm{Re}\left(F_k f e^{-j\theta}\right) \tag{2.8}$$

$$\frac{dp_z}{d\varsigma} = \frac{p_\perp^{s_k}}{p_z}\mathrm{Re}\left(jF_k\frac{df}{d\varsigma}e^{-j\theta}\right) \tag{2.9}$$

$$\frac{d\theta}{d\varsigma} + \frac{w - s_k\Omega_0}{p_z} = -s_k w\frac{p_\perp^{s_k-2}}{p_z}\mathrm{Re}\left[jF_k f e^{-j\theta}\left(f - j\frac{p_z}{w}\frac{df}{d\varsigma}\right)\right] \tag{2.10}$$

where, s_k is harmonic number, p_z is electron axial momentum, $p_\perp$ is electron transverse momentum, Ω_0 is nonrelativistic cyclotron frequency, f designates the axial field variation in the cavity and F_k is normalized field amplitude of the kth mode at the input cavity, which is given as

$$F_k = \frac{eA}{m_0 c\omega_k} \frac{(k_{\perp_k}/k_k)^{s_k-2}}{\Omega_0^{s_k-1}(s_k-1)!2^{s_k+1}} C_{1_k} \tag{2.11}$$

where, $C_{1_k} = \left\{J_{m_k \pm s_k}\left(k_{\perp_k} r_b\right)\right\} \Big/ \left\{\left(x_{m_k n_k}^2 - m_k^2\right) J_{m_k}^2\left(x_{m_k n_k}^2\right)\right\}$, $x_{m_k n_k}$ is the Eigen value of the k^{th} TE mode, ω is angular frequency, e and m_0 are the charge and mass of the electron, m_k is axial index of the k^{th} mode, k is the wave number, r_b is guiding center radius, $k_\perp$ is transverse wave number, '$\pm$' sign in Bessel's function represent co-and counter rotations. The RF input signal amplitude is denoted as $A = \sqrt{4 I_0 P_{in} Q / P_{0\perp} Q_c}$, where, $I_0 = \frac{eI_b}{\gamma_0 m_0 c^3}\left(\frac{1}{(s_k-1)!2^{s_k}}\right)^2 \times \left(\frac{k_{\perp_k}/k_k}{\Omega_0}\right)^{2(s_k-1)} \left(\frac{1}{\int_0^{L_c} f^2 df}\right) C_{1_k}$ is the normalized beam current, P_{in} is RF input power, Q is the quality factor, Q_c is the coupling quality factor, $P_{0\perp} = \left(v_{\perp 0}^2 / 2(1-\gamma_0^{-1})\right) P_b$ is the beam power associated with the gyrating electron at the input end, where, $v_{\perp 0}$ is the initial orbital velocity of the electrons normalized to the velocity of light c, γ_0 is the relativistic factor, $P_b = V_b I_b$ is the beam power, here V_b and I_b are the beam voltage and current, respectively.

2.3.2 Electron Beam Dynamics in the Drift Tube

Electrons enter the drift tube after passing through the cavity, where their energy, momentum, and phase were disrupted by the RF field. Assuming that the radius of the drift tube is small enough, the operating frequency is below the cut-off for all modes, and the evanescent RF field in the drift tube is neglected. However, according to equations (1) - (3), the modulation of electron energy and momentum in the cavity

causes electron phase bunching in the drift tube. The phase bunched electrons leaving the drift tube with the phase,

$$\theta_d = \theta_1 - \int_{L_c}^{L_d} \frac{w_1 - s_1\Omega_0}{p_{z0}} d\varsigma \tag{2.12}$$

where, w_1, p_{z0} and θ_1 are the normalized energy, axial momentum, and phase of the electron at the end of the drift space, L_c is input cavity length and L_d is drift tube length. Since the RF field at the input cavity is small, the perturbations in the drift tube are modest, while minimum perturbations in w_1 and p_z multiplied on the length of the drift tube create a finite change in the electron phase, which leads to the orbital phase bunch of electrons. As a result, the phase, $\theta_d = \bar{\theta}_0 - \Theta_d - X\cos\bar{\theta}_0$ is determined, where Θ_d is the transit angle of unperturbed electrons at drift tube end and $X = 4\frac{p_{\perp 0}^{s_k}}{p_{z0}^2}\frac{F_k}{L_c}\left(\frac{L_c - \Theta_d^2}{\Theta_d^2 - \pi^2}\right)\times\pi\cos\left(\Theta_d/2\right)$ is the bunching parameter, where $p_{\perp 0}$ is normalized transverse momentum.

2.3.3 Electron Beam Dynamics in the Waveguide

Bunched electrons enter into the output cylindrical waveguide region, where they interact with RF field. The electrons interaction with the several TE modes in the output cylindrical waveguide can be illustrated by a self-consistent nonlinear multimode analysis as follows. The RF field component of k^{th} TE mode in the circular waveguide is written as [124]

$$H_{zk} = \mathrm{Re}\left\{A_k(\varsigma)\psi_k e^{j\omega_k t}\right\} \tag{2.13}$$

where $A_k(\varsigma)$ is the axial field distribution of mode k and $\psi_k = J_{m_k}(k_{\perp k}r)e^{-mk\phi}$, ω_k is angular frequency of the kth TE mode, J_{m_k} is first-order Bessel function, $k_{\perp k} = x_{m_k n_k}/r_w$

is transverse wave number of the k^{th} mode, $x_{m_k n_k}$ is the Eigen value of the k^{th} TE mode, r_w is waveguide radius.

The field equation (2.13) indicates an assumption that the existence of the electron beam doesn't affect the transverse field profiles in the output waveguide, and a change of the field amplitude occurs in the axial direction. Substituting the field equation (2.13) into Maxwell's equations, we can obtain the amplitude evolution equation for the beam wave interaction as [124]

$$\left(\frac{d^2}{d\varsigma^2}+k_{zk}^2\right)A_k(\varsigma)=\frac{2I_b k_{\perp k}e}{\pi r_w^2\left[1-\frac{m_k^2}{x_{m_k n_k}^2}\right]J_{m_k}^2\left(x_{m_k n_k}^2\right)}\times\sum_{i=1}^{N}W_i\frac{v_\perp}{v_z}J_{sk}\left(k_{\perp k}r_L\right)J_{mk-sk}\left(k_{\perp k}r_b\right)e^{j\Lambda_i} \quad (2.14)$$

where, $\Lambda_i=s_k\theta_i+\left(m_k-s_k\right)\phi_{ci}-\omega_k t_i$ is the phase distribution, k_{zk} is axial propagation constant, v_z and $v_\perp$ are the axial and transverse velocity of the electron, r_L is Larmor radius, r_b is the beam guiding radius, θ_i is angle of electron position, ϕ_{ci} guiding center angle, I_b is the beam current. W_i is the weighting factor[82] for i th electron, which is defined as $W_i=Ae^{-\left[\left(p_{zi}-\bar{p}_z\right)^2/2\Delta p_z^2\right]}$, it must be satisfy the normalization condition $\sum_{i=1}^{N}W_i=1$, where $\bar{p}_z$ the mean value of axial momentum, Δp_z is the standard deviation from the axial momentum, A is the normalization constant, and N represents the total number of electrons.

The self-consistent electron beam wave interaction in the RF interaction circuit can be specified by the electron motion equation [124]

$$\frac{d\vec{p}}{dt}=-e\vec{v}\times\vec{B}_0-e\left(\vec{E}\times\vec{v}\times\vec{B}\right)+e\vec{B}_0 g\left(\vec{v}\times\vec{r}\right) \quad (2.15)$$

where, $g=\left(1/2\vec{B}_0\right)\left(d\vec{B}_0/d\varsigma\right)$ is a measure of magnetic field tapering, $\vec{p}$ is electron momentum, $\vec{v}$ is electron velocity, $\vec{B}$ and $\vec{E}$ are the magnetic and electric fields of RF wave, B_o is applied magnetic field. The electron motion in the RF interaction section describing the axial momentum $\left(p_z\right)$, transverse momentum $\left(p_\perp\right)$, and the rotation angle $\left(\theta\right)$ is expressed as [21]

$$\frac{dp_z}{d\varsigma}=-m_e cg\frac{\beta_\perp^2}{\beta_z}+\frac{e\mu v_\perp}{v_z}\mathrm{Re}\left\{\sum_k\frac{1}{k_{\perp k}}A_k^{'}\left(\varsigma\right)\times J_{s_k}^{'}\left(k_{\perp k}r_L\right)J_{m_k-s_k}\left(k_\perp r_b\right)e^{j\Lambda_i}\right\} \quad (2.16)$$

$$\frac{dp_\perp}{d\varsigma}=-m_e cg\beta_\perp+\frac{e\mu}{v_z}\mathrm{Re}\left\{\begin{array}{l}\sum_k\frac{1}{k_{\perp k}}\left(i\omega_k A_k\left(\varsigma\right)+v_z A_k^{'}\left(\varsigma\right)\right)\\ \times J_{s_k}^{'}\left(k_{\perp k}r_L\right)J_{m_k-s_k}\left(k_\perp r_b\right)e^{j\Lambda_i}\end{array}\right\} \quad (2.17)$$

$$\frac{d\theta}{d\varsigma}=\frac{eB_0}{p_z}-\frac{\mu e}{wcv_z\beta_\perp}\times\mathrm{Re}\left\{\begin{array}{l}\sum_k\frac{1}{k_{\perp k}^2}\left(\frac{s_k\omega_k}{r_L}A_k^{'}\left(\varsigma\right)-k_{\perp k}^2v_\perp A_k^{'}\left(\varsigma\right)-\frac{is_k}{r_L}v_z A_k^{'}\left(\varsigma\right)\right)\\ \times J_{s_k}^{'}\left(k_{\perp k}r_L\right)J_{m_k-s_k}\left(k_\perp r_b\right)e^{j\Lambda_i}\end{array}\right\} \quad (2.18)$$

where, μ is the permeability, $\beta_{\|}$ is normalized axial velocity, $\beta_\perp$ is the normalized transverse velocity.

2.4. Results and Discussions

In the present work, the beam wave interaction behavior of a *Ka*-band gyro-tystron was investigated using a self-consistent nonlinear multimode analysis. The solution for electron motion and the field generated by electrons is derived by solving a set of self-consistent coupled equations stated in the preceding section. In self-consistent calculations, the equations of motion for the electron and electromagnetic field are solved concurrently; the effect of electron kinematics and field equations on each other is evaluated, and the step size is updated iteratively. Fig. 2. 6 depicts the spatial growth

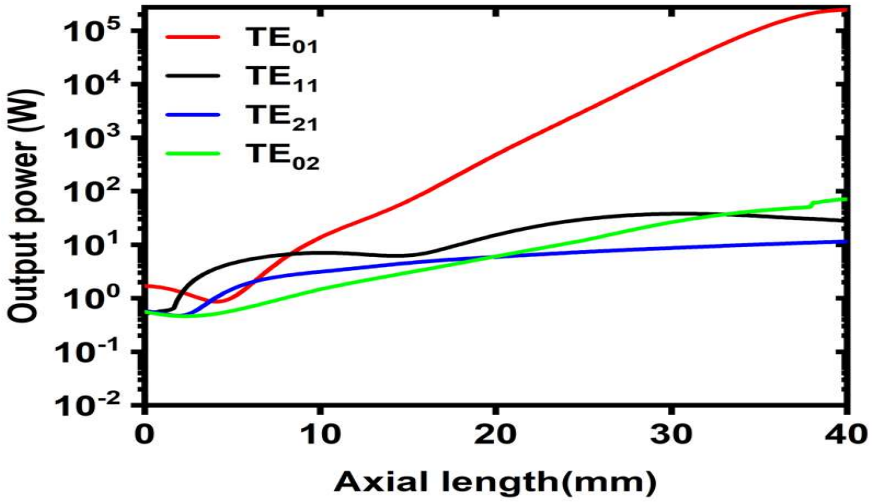

Fig. 2. 6. Output power growth along the length of the waveguide.

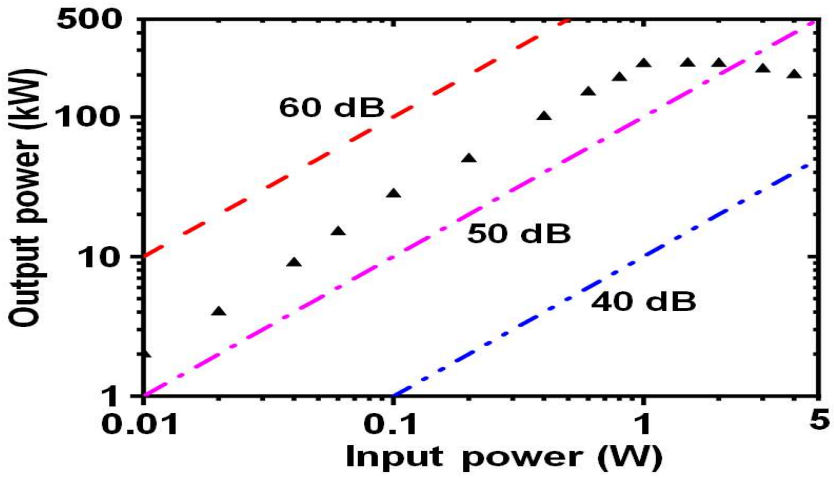

Fig. 2. 7. Transfer characteristics of the single cavity *Ka*- band gyro-twystron.

of RF power in the desired TE_{01} mode and competing TE_{11}, TE_{21}, and TE_{02} modes. According to the nonlinear multimode analysis, the TE_{01} mode at 35 GHz produces 237 kW of RF output power, whereas other competing modes have substantially less power. The gain and electronic efficiency were calculated to be 53 dB and 37%, respectively, employing an electron beam of 65 kV, 10 A, and a velocity ratio of 1.4. The output power and bandwidth of the current amplifier have been calculated at different velocity spreads. The RF output power and 3 dB bandwidth of ~237 kW and ~2GHz are achieved for zero velocity spread. It is observed that the amplifier output power

decreases as the velocity spread increases. Further, by computing the transfer characteristics, as shown in Fig. 2.7, the performance of the current single cavity gyro-twystron is investigated. The transfer characteristics reveal that the output power increases linearly with the input power and is saturated at 1W of the input power. In addition, as the RF input power of the amplifier increases, it does not respond and becomes overdriven; hence, the output power is decreased.

2.5. Conclusion

In the present chapter, the design approach of the *Ka*-band gyro-twystron amplifier has been developed along with the beam wave interaction theory. Each component of a gyro-twystron amplifier, such as the cavity, drift tube, and waveguide, has its design issues addressed. A steady state self-consistent nonlinear multimode analysis was used to investigate the complete RF wave-electron beam interaction behaviour of a *Ka*-band gyro-twystron. In addition, the stability of the amplifier against parasitic oscillations is analyzed and studied using linear theory. The potential capabilities of the single-cavity gyro-twystron have been studied, which provides a broader bandwidth over the gyroklystron and provides better gain and moderate bandwidth as compared to the gyro-TWT. Further, the analytical findings will be verified using a three-dimensional PIC code CST studio suite in chapter 3.